

# Cloud-cloud collision as drivers of the chemical complexity in Galactic Centre molecular clouds

S. Zeng,<sup>1,2,3★</sup> Q. Zhang,<sup>2</sup> I. Jiménez-Serra,<sup>4</sup> B. Tercero,<sup>5,6</sup> X. Lu,<sup>7</sup>  
J. Martín-Pintado,<sup>4</sup> P. de Vicente,<sup>6</sup> V. M. Rivilla,<sup>8</sup> and S. Li<sup>2,9,10</sup>

<sup>1</sup>*School of Physics and Astronomy, Queen Mary University of London, Mile End Road, E1 4NS London, United Kingdom*

<sup>2</sup>*Center for Astrophysics | Harvard & Smithsonian, 60 Garden Street, Cambridge, MA 02138, USA*

<sup>3</sup>*Star and Planet Formation Laboratory, RIKEN Cluster for Pioneering Research, 2-1, Hirosawa, Wako, Saitama 351-0198, Japan*

<sup>4</sup>*Centro de Astrobiología (CSIC/INTA), Ctra. de Torrejón a Ajalvir km 4, Torrejón de Ardoz, 28850 Madrid, Spain*

<sup>5</sup>*Observatorio Astronómico Nacional (OAN-IGN), Calle Alfonso XII, 3, 28014 Madrid, Spain*

<sup>6</sup>*Observatorio de Yebes (IGN), Cerro de la Palera S/N, 19141, Guadalajara*

<sup>7</sup>*National Astronomical Observatory of Japan, 2-21-1 Osawa, Mitaka, Tokyo, 181-8588, Japan*

<sup>8</sup>*INAF-Osservatorio Astrofisico di Arcetri, Largo Enrico Fermi 5, I-50125, Florence, Italy*

<sup>9</sup>*Shanghai Astronomical Observatory, Chinese Academy of Sciences, 80 Nandan Road, Shanghai 200030, China*

<sup>10</sup>*University of Chinese Academy of Sciences, 19A Yuquanlu, Beijing 100049, China*

Accepted XXX. Received YYY; in original form ZZZ

## ABSTRACT

G+0.693-0.03 is a quiescent molecular cloud located within the Sagittarius B2 (Sgr B2) star-forming complex. Recent spectral surveys have shown that it represents one of the most prolific repositories of complex organic species in the Galaxy. The origin of such chemical complexity, along with the small-scale physical structure and properties of G+0.693-0.03, remains a mystery. In this paper, we report the study of multiple molecules with interferometric observations in combination with single-dish data in G+0.693-0.03. Despite the lack of detection of continuum source, we find small-scale (0.2 pc) structures within this cloud. The analysis of the molecular emission of typical shock tracers such as SiO, HNC, and CH<sub>3</sub>OH unveiled two molecular components, peaking at velocities of 57 and 75 km s<sup>-1</sup>. They are found to be interconnected in both space and velocity. The position-velocity diagrams show features that match with the observational signatures of a cloud-cloud collision. Additionally, we detect three series of class I methanol masers known to appear in shocked gas, supporting the cloud-cloud collision scenario. From the maser emission we provide constraints on the gas kinetic temperatures (~30-150 K) and H<sub>2</sub> densities (10<sup>4</sup>-10<sup>5</sup> cm<sup>-2</sup>). These properties are similar to those found for the starburst galaxy NGC253 also using class I methanol masers, suggested to be associated with a cloud-cloud collision. We conclude that shocks driven by the possible cloud-cloud collision is likely the most important mechanism responsible for the high level of chemical complexity observed in G+0.693-0.03.

**Key words:** Galaxy: centre – ISM: molecules – ISM: kinematics and dynamics – ISM: clouds

## 1 INTRODUCTION

The inner ~500 pc of the Milky Way is known as the Central Molecular Zone (or CMZ). It is a heavily processed region and a hotbed of star formation activity, containing the most extreme massive star formation sites (Morris & Serabyn 1996) in our Galaxy. A significant part of the molecular

gas in the CMZ, however, is found in quiescent giant molecular clouds (GMCs), which exhibit a high level of turbulence (highly supersonic) and little, or non-existent, star formation activity (e.g. Longmore et al. 2013; Kauffmann et al. 2017; Lu et al. 2019b,a). In contrast to GMCs in the Galactic disk, GMCs in the CMZ are exposed to energetic phenomena such as shock waves (due to the high level of turbulence), intense UV radiation fields (from nearby massive stellar clusters such as the Arches and the Quintuplet clusters), X-rays

★ E-mail: shaoshan.zeng@riken.jp

(coming from the central and massive black hole) and enhanced cosmic-ray ionisation rates (e.g. Bally et al. 1987a; Koyama et al. 1989; Goto et al. 2013; Yusef-Zadeh et al. 2013; see also Mills et al. 2018, and references therein). The physical conditions of the CMZ molecular clouds therefore differ substantially from the rest of the Galaxy. Indeed, the average  $\text{H}_2$  gas density ( $\sim 10^4 \text{ cm}^{-3}$ , Guesten & Henkel 1983; Bally et al. 1987b; Rodríguez-Fernández et al. 2000) is several orders of magnitude above the average in the Galactic disc, and the gas temperature typically ranges between  $\sim 30 \text{ K}$  to  $\sim 150 \text{ K}$ , (Huettemeister et al. 1993; Guesten et al. 1985; Ott et al. 2014; Ginsburg et al. 2016; Krieger et al. 2017). The gas temperature is decoupled from the much lower temperature of dust grains of  $\leq 20 \text{ K}$  (Rodríguez-Fernández et al. 2004; Nagayama et al. 2009).

One molecular cloud that stands out over the others within the CMZ is designated by its Galactic coordinates as G+0.693-0.03 (hereafter G+0.693). Single-dish spectral surveys performed with the IRAM 30m and GBT telescopes have revealed a plethora of molecular species including many complex organic molecules (COMs) in the region of G+0.693 (Requena-Torres et al. 2008; Zeng et al. 2018; Rivilla et al. 2018, 2019; Jimenez-Serra et al. 2020). It is believed that G+0.693 represents one of the largest molecular repositories of COMs in our Galaxy (Requena-Torres et al. 2006, 2008). G+0.693 can be found within the Sagittarius B2 (Sgr B2 hereafter) star-forming cloud, which is known to be one of the most active sites of star formation in our Galaxy. As a whole, Sgr B2 can be distinguished into three different parts: a low-density envelope, a moderate density region, and the most compact, densest molecular regions (as illustrated in Schmiedeke et al. 2016).

At the centre of the envelope, three sources named according to their relative location in an equatorial coordinate system, Sgr B2(North), Sgr B2(Main), and Sgr B2(South), are positioned along a north-south ridge. Especially, the former two are well-known sites for active star formation that comprise all the typical signposts of massive star formation such as, hot cores, molecular masers of  $\text{H}_2\text{O}$ , OH,  $\text{H}_2\text{CO}$ ,  $\text{CH}_3\text{OH}$ , and SiO, and ultra-compact H II regions (see e.g. Martín-Pintado et al. 1999; De Vicente et al. 2000; Jones et al. 2008, and references therein). The morphology and kinematic features identified in Sgr B2 have been interpreted as the result of a cloud-cloud collision (Hasegawa et al. 1994, 2008; Sato et al. 2000; Tsuboi et al. 2015), which possibly triggered this intense star-formation activity.

Considering Sgr B2N is at an earlier stage of star formation than Sgr B2M (Miao et al. 1995; De Vicente et al. 2000), one might postulate that the star formation activity occurs sequentially from Sgr B2M to north. If this is the case, early star formation activity is also expected in G+0.693 since it is located also at the ridge just only  $\sim 55''$  north-east away from Sgr B2N. However, signposts of ongoing star formation such as UC H II regions,  $\text{H}_2\text{O}$  masers, class II  $\text{CH}_3\text{OH}$  masers, or  $\text{H}_2\text{CO}$  masers or even precursors of massive star formation such as dust continuum sources have not yet been detected toward G+0.693 (Ginsburg et al. 2018; Lu et al. 2019a). The nature of G+0.693 remains quiescent. Recent star formation of intermediate ( $2-8 M_\odot$ ) and high-mass stars ( $>8 M_\odot$ ) can however be masked even in high-sensitivity continuum observations by large amounts of dust in deeply embedded molecular clouds, as found for the intermediate

mass hot core found in the Cepheus A HW2 system (see e.g. Martín-Pintado et al. 2005; Jiménez-Serra et al. 2009). Therefore, if present, high-angular resolution observations of rotational molecular lines are better probes of young massive star formation in the form of intermediate- and high-mass hot molecular cores (Jiménez-Serra et al. 2007, 2009). In fact, the presence of hot core-like sources in G+0.693 would explain the high level of chemical complexity found in this source, with over 40 COMs detected including the prebiotic molecules cyanomethanimine and urea (Requena-Torres et al. 2008; Zeng et al. 2018; Rivilla et al. 2019; Jimenez-Serra et al. 2020). Up to date, there are more than 200 molecules that have been detected in the ISM of which about one third of them ( $\sim 70$ ) are COMs (molecules containing 6 or more atoms)<sup>1</sup>. G+0.693 is therefore an ideal candidate to improve our understanding of the origin of COMs in the ISM.

Besides, the chemical richness observed in G+0.693 could also be related to the presence of large-scale, low-velocity shocks that populate the Galactic Centre. In low-velocity shocks (with shock velocity of  $\sim 20 \text{ km s}^{-1}$ ), dust grains are efficiently sputtered, fully releasing the materials present in the icy mantles (including COMs), and partially eroding grain cores (see e.g. Jiménez-Serra et al. 2008). This is consistent with widespread SiO emission detected across the Galactic Centre (Martín-Pintado et al. 1997). Additional support for the shock scenario comes from the detection of class I methanol masers in the region (see Liechti & Wilson 1996; Jones et al. 2011). Usually Class I methanol masers are formed in regions of recent star formation associated with outflow activity. It is believed that the physical conditions and the  $\text{CH}_3\text{OH}$  abundance required for this type of masers in the material has experienced shock interaction (e.g. Voronkov et al. 2006; Cyganowski et al. 2009; Pihlström et al. 2014).

The origin of a large-scale, low-velocity shock in the quiescent GMC G+0.693 is unknown. Two scenarios have been proposed: 1) the shocks in G+0.693 could be produced by small-scale expanding wind-blown bubbles driven by evolved massive stars (Martín-Pintado et al. 1999); or 2) these shocks are associated with a large-scale cloud-cloud collision, as mentioned earlier. Henshaw et al. (2016) investigated the large-scale kinematics of Sgr B2N complex and identified a conical profile of Sgr B2 in the position-position-velocity space (see their Figure 17). This feature coincides with the location of G+0.693 where two gas streams could be merging into a cloud-cloud collision, consistent with the second hypothesis. Other interpretations are related to the global orbital structure of the molecular gas in the CMZ, or a signature of global collapse (J.Henshaw, private communication).

With the purpose of understanding the origin of COMs in G+0.693 i.e. the main mechanism(s) responsible for the peculiar chemistry observed, we have used interferometric submillimeter observations of several rotational molecular lines to gain insight into the morphology, the kinematics, and the physical properties of G+0.693 at small scales, which have not been studied in detail before. We also report the detection of a series of class I methanol masers, usually as-

<sup>1</sup> <https://cdms.astro.uni-koeln.de/classic/molecules>

sociated with shocks, toward this source by using single-dish telescopes which provide constraints on the physical properties of the shocked gas experiencing the maser amplification. This paper is distributed as follows: Section 2 describes the data used throughout this study. The main results are depicted and discussed in Section 3 and 4. Throughout this study, we adopt a distance to the Galactic Centre of 8.4 kpc (Reid et al. 2014).

## 2 OBSERVATIONS

### 2.1 Submillimeter Array (SMA) observations

We used the archival Submillimeter Array (SMA)<sup>2</sup> data in the compact configuration from CMZoom survey (project code: 2013B-S091, PIs: C.Battersby and E. Keto; Battersby et al. 2017, 2020) and sub-compact configuration (project code: 2013B-S055) to study the small-scale morphology and kinematics of G+0.693. The data set is a six-pointing mosaic around the position of G+0.693 observed at the 230 GHz band in 2014. The primary beam of SMA is  $\sim 55''$  at the observed frequency. A total bandwidth of 8 GHz is covered in two sidebands: rest frequencies of 216.9–220.8 GHz covered in the lower sideband whilst 228.9–232.9 GHz covered in the upper sideband. The continuum data were also obtained within the same observation by averaging line-free spectral channels over the 8 GHz bandwidth. The typical spectral resolution is 0.812 MHz which is equivalent to a velocity resolution of  $\sim 1.1 \text{ km s}^{-1}$ .

Data calibration was carried out in MIR<sup>3</sup> and MIRIAD (Sault et al. 1995). Spectral lines and continuum were subsequently imaged and analysed using CASA (McMullin et al. 2007). A 1.3 mm continuum map was generated averaging channels free of line emission. The resulting image has a synthesised beam of  $4''.0 \times 3''.7$  (equivalent to  $0.16 \text{ pc} \times 0.14 \text{ pc}$ ) with a position angle of  $30^\circ.2$ . Each of the detected molecular lines was imaged separately. The line maps have a typical synthesised beam of  $\sim 4''.4 \times 4''.0$  (equivalent to  $0.18 \text{ pc} \times 0.16 \text{ pc}$ ) with a position angle of  $33^\circ.7$ . The rms of continuum map and spectral line maps is  $\sim 5 \text{ mJy beam}^{-1}$  and  $\sim 0.2 \text{ Jy beam}^{-1}$  per  $1.1 \text{ km s}^{-1}$  channel respectively.

### 2.2 Atacama Pathfinder EXperiment (APEX) data

For the spectral lines, we also utilised the single-dish data observed with Atacama Pathfinder EXperiment (APEX) (Ginsburg et al. 2016) at 216.9–220.9 GHz which covers the same frequency range as the lower sideband of our SMA observation. However, no single-dish data are available to cover the same frequency range as the upper sideband (228.9–232.9 GHz). Hence molecules detected in the upper sideband will not be imaged and analysed.

Although the SMA observations were performed in both

compact and sub-compact configurations, the data still suffer from missing flux due to limited uv-coverage of short baselines of the interferometer. To account for this, we combined the SMA interferometric data with the APEX single-dish data by employing the *feather* task in CASA. All the maps presented in this work are not corrected for primary-beam response in order to have a uniform rms level across the maps.

### 2.3 Single-dish observations with Yebes 40m, IRAM 30m and GBT telescope

The observations of the class I methanol masers at 36.169 GHz and at 44.069 GHz were carried out with the Yebes 40m telescope<sup>4</sup> (de Vicente et al. 2016) located at 990 m of altitude in Yebes (Guadalajara, Spain), during 6 observing sessions in February 2020. The equatorial coordinates of the G+0.693 source were  $\alpha_{J2000} = 17^{\text{h}} 47^{\text{m}} 22^{\text{s}}$ ,  $\delta_{J2000} = -28^\circ 21' 27''$ . Due to the low declination of the source and the Yebes latitude ( $+40^\circ 31' 29.6''$ ), the source was only 5 hours above an elevation of  $15^\circ$  per observing session, reaching a maximum elevation of  $21^\circ$ . We used the new Q band (7 mm) HEMT receiver that allows broad-band observations in two linear polarizations. The receiver is connected to 16 fast Fourier transform spectrometers (FFTS) with 2.5 GHz of spectral coverage and 38 kHz of spectral resolution. This system provides an instantaneous bandwidth of 18 GHz per polarization in the frequency range between 31.5 GHz and 50 GHz (F. Tercero et al. in preparation). The intensity scale was calibrated using two absorbers at different temperatures and the atmospheric transmission model (ATM, Cernicharo 1985; Pardo et al. 2001).

The observational procedure was position switching mode with the reference position located at  $\Delta\alpha = -885''$  and  $\Delta\delta = +290''$  with respect to G+0.693. The telescope pointing and focus were checked every one or two hours through pseudo-continuum observations towards VX Sgr, a red hypergiant star near the target source, with strong SiO  $v=1 \ J=1-0$  (at 43.122 GHz) maser emission. Pointing errors were always kept within  $5''$  in both axes.

The spectra were measured in units of antenna temperature,  $T_A^*$ , and corrected for atmospheric absorption and spillover losses. At 36 GHz, system temperatures were in the range 75–180 K depending on the observing session (with pressure water vapour ranging from 6 mm to 10 mm) and source elevation (from  $15^\circ$  to  $20^\circ$ ). At this frequency, the aperture efficiency, the conversion factor between flux ( $S$ ) and antenna temperature ( $T_A^*$ ), and the half power beam width (HPBW) of the Yebes 40m telescope are respectively 0.43, 4.6 Jy/K, and  $48''$ .

In addition, we also used a spectral line survey toward G+0.693 performed with the IRAM 30m telescope at Pico Veleta<sup>5</sup> (Spain) and the NRAO<sup>6</sup> 100m Robert C. Byrd Green Bank telescope (GBT) in West Virginia (USA),

<sup>2</sup> The SMA is a joint project between the Smithsonian Astrophysical Observatory and the Academia Sinica Institute of Astronomy and Astrophysics and is funded by the Smithsonian Institution and the Academia Sinica.

<sup>3</sup> MIR is an IDL-based package developed to calibrate SMA data (Available at <https://www.cfa.harvard.edu/cqi/mircook.html>).

<sup>4</sup> [http://rt40m.oan.es/rt40m\\_en.php](http://rt40m.oan.es/rt40m_en.php)

<sup>5</sup> IRAM is supported by INSU/CNRS (France), MPG (Germany), and IGN (Spain).

<sup>6</sup> The National Radio Astronomy Observatories is a facility of the National Science Foundation, operated under a cooperative agreement by Associated Universities, Inc.

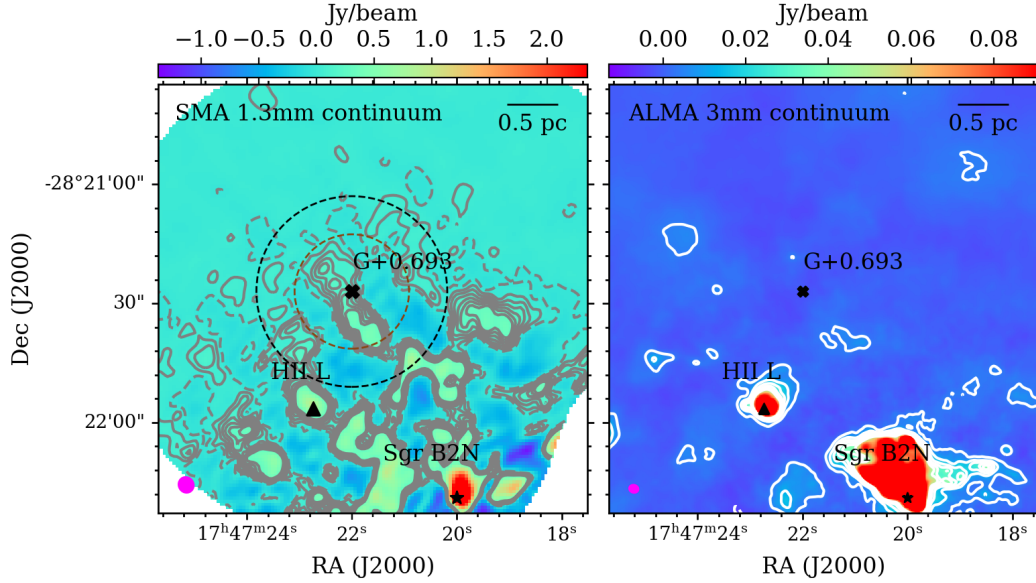


**Figure 1.** Left: SMA 1.3 mm continuum map centred at the position of G+0.693. Grey solid contours represent  $5\sigma$ - $55\sigma$  levels in steps of  $10\sigma$ , where  $1\sigma=5$  mJy/beam whilst grey dashed contour represents  $-5\sigma$  level. The SMA synthesised beam,  $4''.0 \times 3''.7$  with a position angle of  $30^\circ.2$ , is shown in the lower-left corner. The black cross, triangle and star symbol indicate the position of G+0.693, HII region L, and Sgr B2N respectively. The brown and black dashed circle indicate respectively the largest beam size ( $\sim 29''$ ) of IRAM 30 m observations and Yebes 40 m ( $\sim 48''$ ) observations toward G+0.693. Right: ALMA 3 mm continuum map from Ginsburg et al. (2018) centred at the position of G+0.693. White contours represent  $5\sigma$ - $55\sigma$  levels in steps of  $10\sigma$ , where  $1\sigma=0.78$  mJy/beam. The synthesised beam,  $2''.35 \times 1''.99$  with a position angle of  $74^\circ.6$ , is shown in the lower-left corner. The label for each source is the same as left panel.

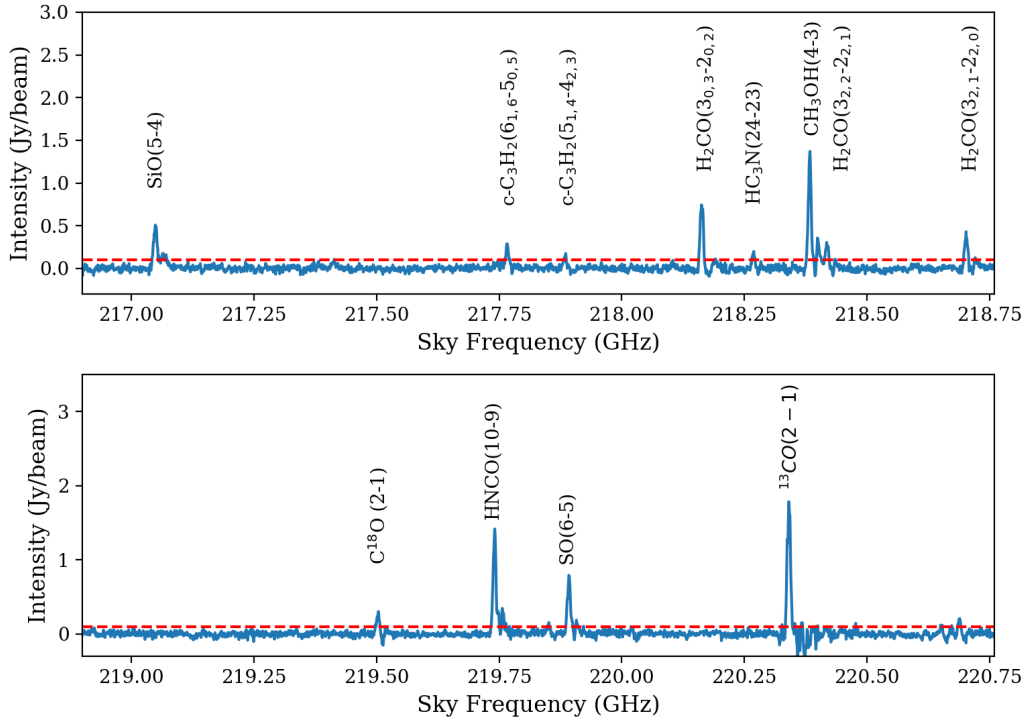


**Figure 2.** Full spectra measured between 216.9-218.8 GHz (upper panel) and 218.9-220.8GHz (lower panel) in the lower sideband of the SMA observations. Detected molecular species are identified and labelled with their name and transition. Horizontal red dashed line marks the  $3\sigma$  level.



covering frequencies from 12 to 272 GHz. The observations were centred at the coordinates  $\alpha_{J2000} = 17^h 47^m 22^s$ ,  $\delta_{J2000} = -28^\circ 21' 27''$ . We refer to [Zeng et al. \(2018\)](#) for more detailed information on the observations.

### 3 RESULTS

#### 3.1 The 1.3 mm continuum map

The continuum map made with only the SMA data is shown in left panel of Figure 1. The pointing position of G+0.693 ( $\alpha(J2000.0) = 17^h 47^m 22^s$  and  $\delta(J2000.0) = -28^\circ 21' 27''$ ) used in previous IRAM 30 m surveys (see e.g. [Zeng et al. 2018](#)) is indicated by a black cross. Consistent with the non-detection of ALMA 3 mm continuum emission in the Sgr B2M and N region recently reported by [Ginsburg et al. \(2018, see right panel of Figure 1\)](#), no clear continuum peak is detected with the SMA at 1.3 mm toward the position of G+0.693. This supports the idea that no massive star formation is taking place within the cloud. To estimate an upper limit to the mass of any possible protostellar core present in the source, we use the following equation:

$$M = \frac{F_\nu d^2}{B_\nu(T_{\text{dust}})\kappa_\nu} \frac{M_{\text{gas}}}{M_{\text{dust}}} \quad (1)$$

where  $\frac{M_{\text{gas}}}{M_{\text{dust}}}$  is the gas-to-dust mass ratio,  $F_\nu$  is the continuum flux,  $d$  is the distance to the target,  $B_\nu(T_{\text{dust}})$  is the Planck function at dust temperature  $T_{\text{dust}}$ , and  $\kappa_\nu$  is the dust opacity. We assumed  $\frac{M_{\text{gas}}}{M_{\text{dust}}} = 100$ ,  $d = 8.4$  kpc,  $T_{\text{dust}} = 20$  K determined from [Rodríguez-Fernández et al. \(2004\)](#); [Nagayama et al. \(2009\)](#), and  $\kappa_\nu = 0.899 \text{ cm}^2 \text{ g}^{-1}$  (MRN model with thin ice mantles, after  $10^5$  years of coagulation at densities of  $10^6 \text{ cm}^{-3}$ ; [Ossenkopf & Henning 1994](#)<sup>7</sup>). From the  $3\sigma$  rms noise level measured in our SMA 1.3mm continuum image (15 mJy), we derive an upper limit to the mass of the proto-stellar envelope of  $\leq 2.3 M_\odot$ . This value is above the typical lower limit of low-mass Class 0 and I envelope masses ( $>0.5 M_\odot$ ; [Arce & Sargent 2006](#)), which means that either a low-mass or an intermediate-mass embedded source may exist. To provide further constraints, we carried out the same calculation for the more sensitive ALMA 3 mm continuum from [Ginsburg et al. \(2018\)](#) (see Figure 1). From the  $3\sigma$  rms noise level (2.3 mJy), we derive a proto-stellar envelope mass  $\leq 0.36 M_\odot$ , which is below the lower limit of Class 0 envelope masses. This confirms that G+0.693 is quiescent and rules out the possibility that the origin of the molecular complexity found in G+0.693 is due to hidden star-formation.

#### 3.2 Molecular distributions

As summarised in Table 1, 12 molecular lines were detected in G+0.693 by the combination of SMA and APEX observations. Spectra of the SMA-only full 4 GHz lower sideband are

**Table 1.** Parameters of detected molecular lines.

Molecule	Transition	Rest Frequency (GHz)	$E_{\text{up}}$ (K)
SMA+APEX			
SiO	J=5-4	217.1050	31.26
c-C <sub>3</sub> H <sub>2</sub>	J <sub>Ka,Kc</sub> =6 <sub>1,6</sub> -5 <sub>0,5</sub>	217.8221	38.60
c-C <sub>3</sub> H <sub>2</sub>	J <sub>Ka,Kc</sub> =5 <sub>1,4</sub> -4 <sub>2,3</sub>	217.9400	35.41
H <sub>2</sub> CO	J <sub>Ka,Kc</sub> =3 <sub>0,3</sub> -2 <sub>0,2</sub>	218.2222	20.96
CH <sub>3</sub> OH	J=4 <sub>2</sub> -3 <sub>1</sub>	218.4401	45.46
H <sub>2</sub> CO	J <sub>Ka,Kc</sub> =3 <sub>2,2</sub> -2 <sub>2,1</sub>	218.4756	68.09
HC <sub>3</sub> N	J=24-23	218.3247	130.98
H <sub>2</sub> CO	J <sub>Ka,Kc</sub> =3 <sub>2,1</sub> -2 <sub>2,0</sub>	218.7601	68.11
C <sup>18</sup> O	J=2-1	219.5603	15.80
HNCO	J=10-9	219.7983	58.02
SO	J=6=5	219.9494	34.98
<sup>13</sup> CO	J=2-1	220.3986	15.86
GBT			
CH <sub>3</sub> OH	J <sub>Ka</sub> =3 <sub>2</sub> -3 <sub>1</sub> E	24.9287	36.17
CH <sub>3</sub> OH	J <sub>Ka</sub> =4 <sub>2</sub> -4 <sub>1</sub> E	24.9335	45.46
CH <sub>3</sub> OH	J <sub>Ka</sub> =2 <sub>2</sub> -2 <sub>1</sub> E	24.9344	29.21
CH <sub>3</sub> OH	J <sub>Ka</sub> =5 <sub>2</sub> -5 <sub>1</sub> E	24.9591	57.07
CH <sub>3</sub> OH	J <sub>Ka</sub> =6 <sub>2</sub> -6 <sub>1</sub> E	25.0181	71.00
Yebes 40m			
CH <sub>3</sub> OH	J <sub>Ka</sub> =4 <sub>1</sub> -3 <sub>0</sub> E	36.1692	28.79
CH <sub>3</sub> OH	J <sub>Ka</sub> =7 <sub>0</sub> -6 <sub>1</sub> A	44.0693	64.98
IRAM 30m			
CH <sub>3</sub> OH	J <sub>Ka</sub> =5 <sub>1</sub> -4 <sub>0</sub> E	84.5211	40.39
CH <sub>3</sub> OH	J <sub>Ka</sub> =8 <sub>0</sub> -7 <sub>1</sub> A	95.1693	83.54
CH <sub>3</sub> OH	J <sub>Ka</sub> =6 <sub>1</sub> -5 <sub>0</sub> E	132.8907	54.31
CH <sub>3</sub> OH	J <sub>Ka</sub> =8 <sub>1</sub> -7 <sub>0</sub> E	229.7587	89.10

The parameters are taken from the Jet Propulsion Laboratory (JPL) molecular catalog<sup>8</sup> ([Pickett et al. 1998](#)) and the Cologne Database for Molecular Spectroscopy (CDMS)<sup>9</sup> ([Müller et al. 2001, 2005; Endres et al. 2016](#)).

presented in Figure 2. We note that for most of the molecular species analysed here, we only have one detected transition each detected in our dataset. This does not allow us to accurately determine the abundances of these molecules toward this source. This aspect of the analysis will be covered in a forthcoming paper using higher-sensitivity single-dish surveys carried out toward G+0.693 with the IRAM 30m and the Yebes 40m telescopes. Although <sup>13</sup>CO (J=2-1) is detected toward G+0.693, it is excluded from the analysis as its emission is ubiquitous in the region and its spatial distribution cannot be distinguished between G+0.693 and Sgr B2N. Note that for c-C<sub>3</sub>H<sub>2</sub>(5<sub>1,4</sub>-4<sub>2,3</sub>), HC<sub>3</sub>N, and C<sup>18</sup>O, their emissions are not strong enough to show significant kinematic feature in the emission map, hence they will also be excluded from the analysis. Among the rest of the detected lines, we show in Figure 3 their velocity-integrated intensity, represented by the zeroth-moment maps. The maps were made by integrating the molecular emission over a velocity range between  $\sim 50$  and  $\sim 90 \text{ km s}^{-1}$ . The overall distribution of molecular gas is extended and generally show an elongated morphology which stretches along the north-south

<sup>7</sup> In the GC, most of the ices have been released into the gas phase because of the shocks, so it is not expected that much of the ices remains in solid state.

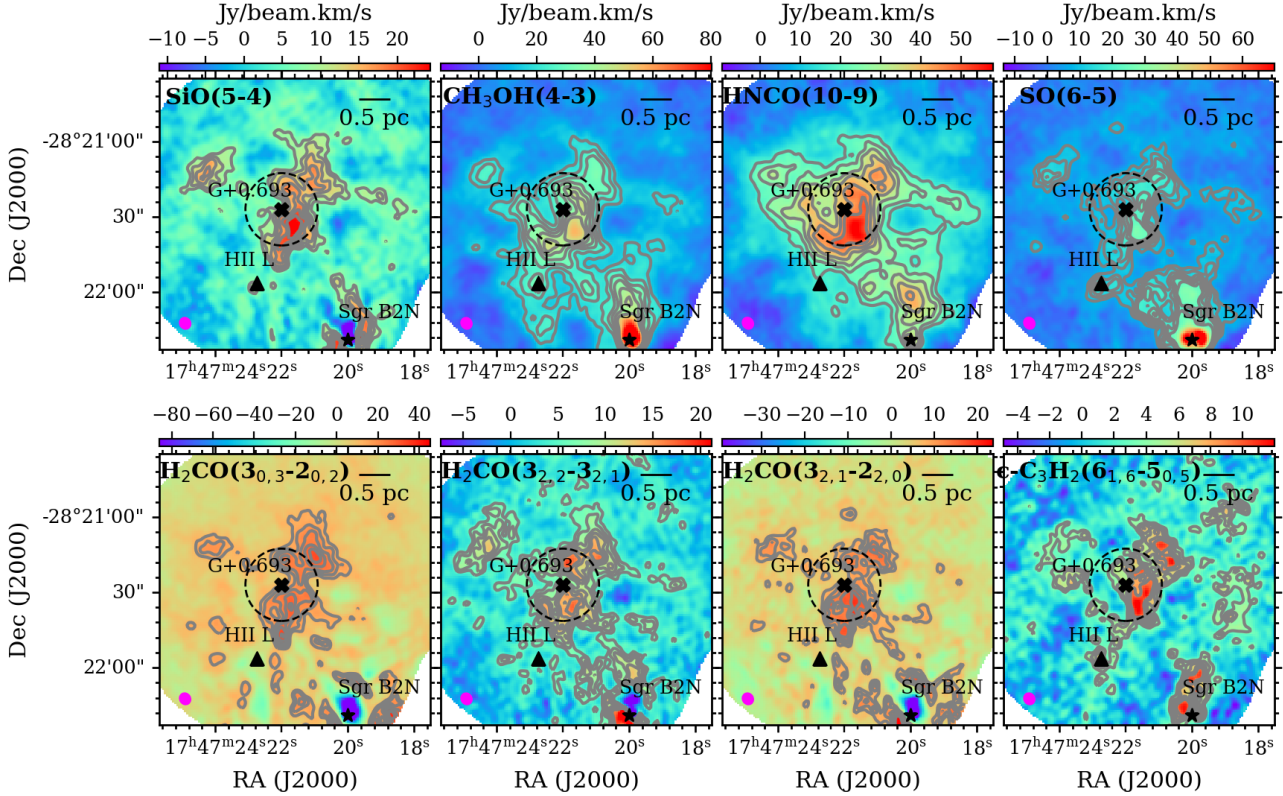


**Figure 3.** Integrated intensity (moment zeroth) maps of all the detected molecular lines in G+0.693 obtained from the merged SMA+APEX datacubes. The synthesised beam ( $4''.4 \times 4''.0$  with a position angle of  $33^\circ.7$ ) is shown as a fuchsia ellipse in the bottom left corner. The dashed circle in each panel indicates the beam size ( $\sim 29''$ ) of previous IRAM 30 m observations toward G+0.693. Grey contour levels represent 30%-80%, in the step of 10%, of the molecular peak. The location of Sgr B2N, G+0.693, and HII region L are labelled as Figure 1.

direction. In particular, strong molecular emission tend to distribute in an arch shape that surrounds the west side of G+0.693. Moreover, a molecular condensation is clearly seen in the same off-position,  $\sim 5''$  ( $\sim 0.2$  pc) south-west away from the pointing position of G+0.693. Given that the beam size of the IRAM 30 m observations is  $\sim 29''$  (indicated by a dashed circle in Figure 3), this shift in the peak position of molecular emissions is conceivable and may imply the presence of smaller-scale structure that has never been observed previously. Furthermore, the observed condensation might be a density enhancement produced by shocked gas which might represent the precursor of massive star-forming regions. The relatively strong emission of well-known shock tracers such as SiO, CH<sub>3</sub>OH, HNC, and SO is shown to be tracing the shocked materials around G+0.693. This further supports the proposed mechanism that wealth of COMs observed toward G+0.693 is likely due to widespread shocks sputtering off grain mantles, releasing molecular species into the gas phase (Martín-Pintado et al. 1997; Requena-Torres et al. 2006).

In the following, we will mainly focus on the shock tracers: HNC, SiO, CH<sub>3</sub>OH, and SO, detected in our dataset to investigate the kinematics of G+0.693. In Figure 4, we present the integrated intensity maps of SiO, CH<sub>3</sub>OH, HNC, and SO at four different velocity ranges (i.e. 50-60,

60-70, 70-80, and 80-90 km s<sup>-1</sup>). At 50-60 km s<sup>-1</sup>, molecular gas is distributed mainly on the east side in regard to the position of G+0.693. On the other hand, the prominent emission peak seen in Figure 3 distinctly appears on the west side at 70-90 km s<sup>-1</sup>. The entangled gas distribution present at 60-70 km s<sup>-1</sup> may indicate that the lower and higher velocity components are merged at this intermediate velocity range. We hereafter refer the component at 50-60 km s<sup>-1</sup> 'blue-shifted component' and the component at 70-90 km s<sup>-1</sup> 'red-shifted component'. In Figure 5(a), the blue-shifted component and red-shifted component (blue and red contour respectively) are superimposed on the CH<sub>3</sub>OH integrated intensity map (colour scale). We also include the same figure for HNC, SO, and SiO emission in the Appendix as supplementary materials. It is interesting to note that the northern and the southern part of these two components are spatially overlapping while the middle region is apart from each other. Since we have combined the SMA observation with the APEX data, this middle region is not caused by missing flux of the interferometric data. To further examine the two velocity components, we display the spectra toward our selected four small areas highlighted by the respective box in Figure 5(a). Note that box 1 and 3 are chosen at the southern and the northern region where two clouds are overlapped; box 2 is chosen at the molecular peak

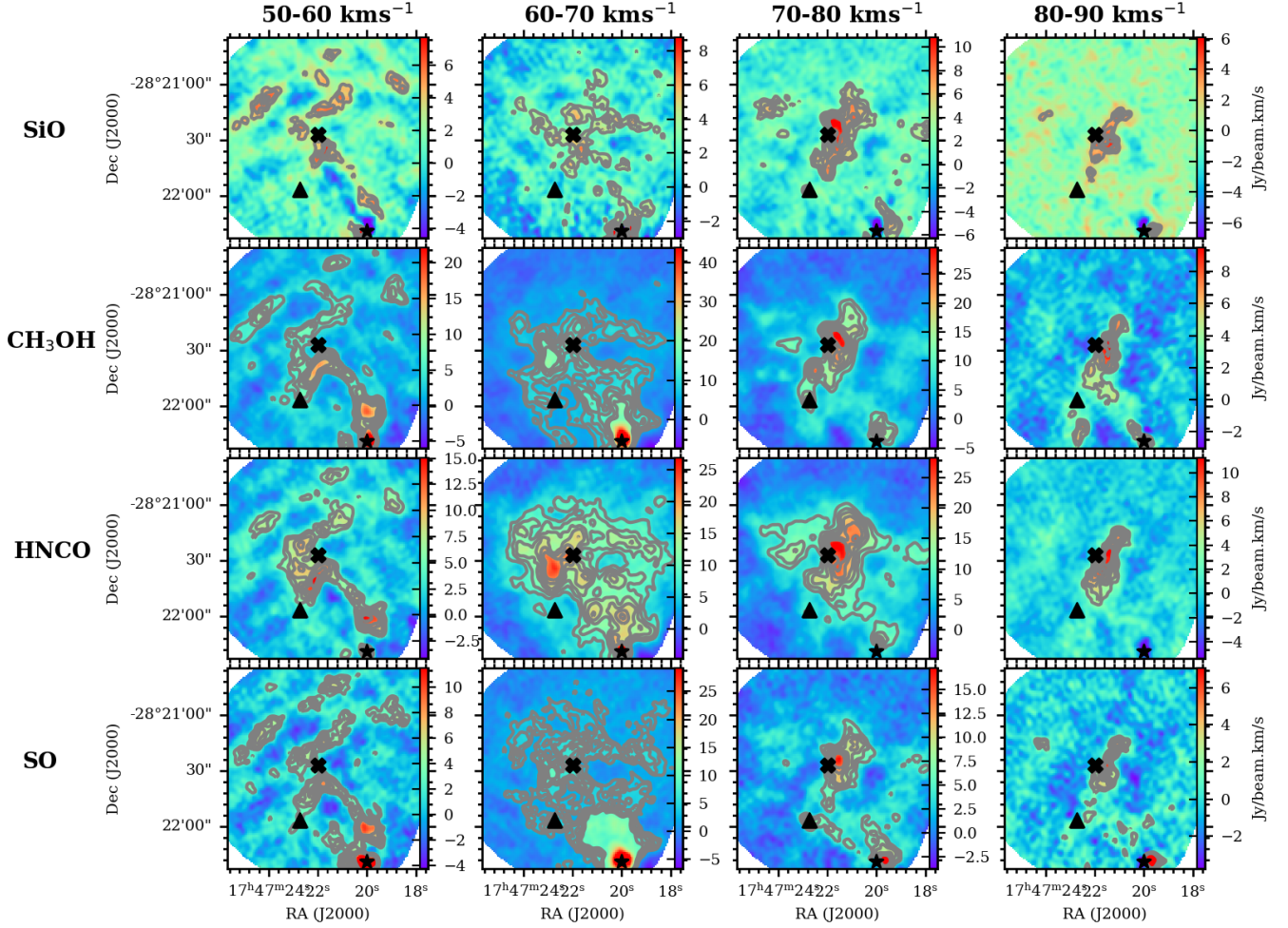


**Figure 4.** Velocity channel distributions of SiO(5-4), CH<sub>3</sub>OH(4-3), HNC(10-9), and SO(6-5) emission at velocity step of 10 km s<sup>-1</sup>. In each panel, the contour levels represent 30%-80%, in the step of 10%, of the molecular peak.

observed in zeroth-moment maps (see Figure 3); box 4 is chosen at an area where two clouds are apart from each other. Each spectrum is obtained by averaging each area (see Figure 5(b) - (e)). For the spectrum obtained from areas where the blue-shifted component and the red-shifted component is overlapped (i.e. box 1, 2, and 3), the two velocity components centred at  $\sim 57$  km s<sup>-1</sup> and  $\sim 75$  km s<sup>-1</sup> are presented along with an almost flattened profile between two velocity peaks. The latter can be interpreted as the so-called 'bridge feature', an observational signature of cloud-cloud collision, at the intermediate velocity range which can also be seen in a position-velocity diagram (more details in Discussions). Indeed, the position-velocity diagrams of CH<sub>3</sub>OH (see Figure 5 (f) and (g)) depict consistently the bridge feature connecting the two clouds in velocity space. This feature is also noticeable in the positive-velocity diagrams of other shock tracers (see Figure A1-A3 in Appendix).

### 3.3 Methanol maser lines in G+0.693

Class I methanol masers are considered as good tracers of outflow activity in star-forming regions. It is remarkable that a rather strong class I methanol maser is detected in

G+0.693 where no star formation is taken place. Therefore, the class I methanol maser is unlikely to be associated with outflow activity. Indeed, unlike outflows, the methanol maser emission at 36 GHz is extended over several parsecs across the SgrB2 complex (see Liechti & Wilson 1996; Jones et al. 2011), which suggests that the physical conditions in the large scale shocks give rise to the class I methanol maser in the Sgr B2 region. Using the Yebes 40m telescope, we have detected the two well-known class I methanol maser lines 4<sub>-1</sub> - 3<sub>0</sub> E and 7<sub>0</sub> - 6<sub>1</sub> A at 36.2 GHz and 44.1 GHz respectively toward G+0.693. Together with the spectral line surveys obtained with GBT and IRAM 30m telescope, 11 class I methanol maser lines in total are identified toward G+0.693 (see Table 1). They can be categorised into three families: the J<sub>2</sub> - J<sub>1</sub> E series, the (J+1)<sub>-1</sub> - J<sub>0</sub> E series, and the (J+1)<sub>0</sub> - J<sub>1</sub> A series (Leurini et al. 2016). All the line profiles of the detected class I methanol maser lines are presented in Figure 6. Owing to the larger beam sizes of GBT, IRAM 30m, and Yebes 40m observations, the presence of two velocity components are not as clear as that shown in the SMA+APEX data, but they seem to appear at the same corresponding velocity range, most notable in (J+1)<sub>0</sub> - J<sub>1</sub> A series.



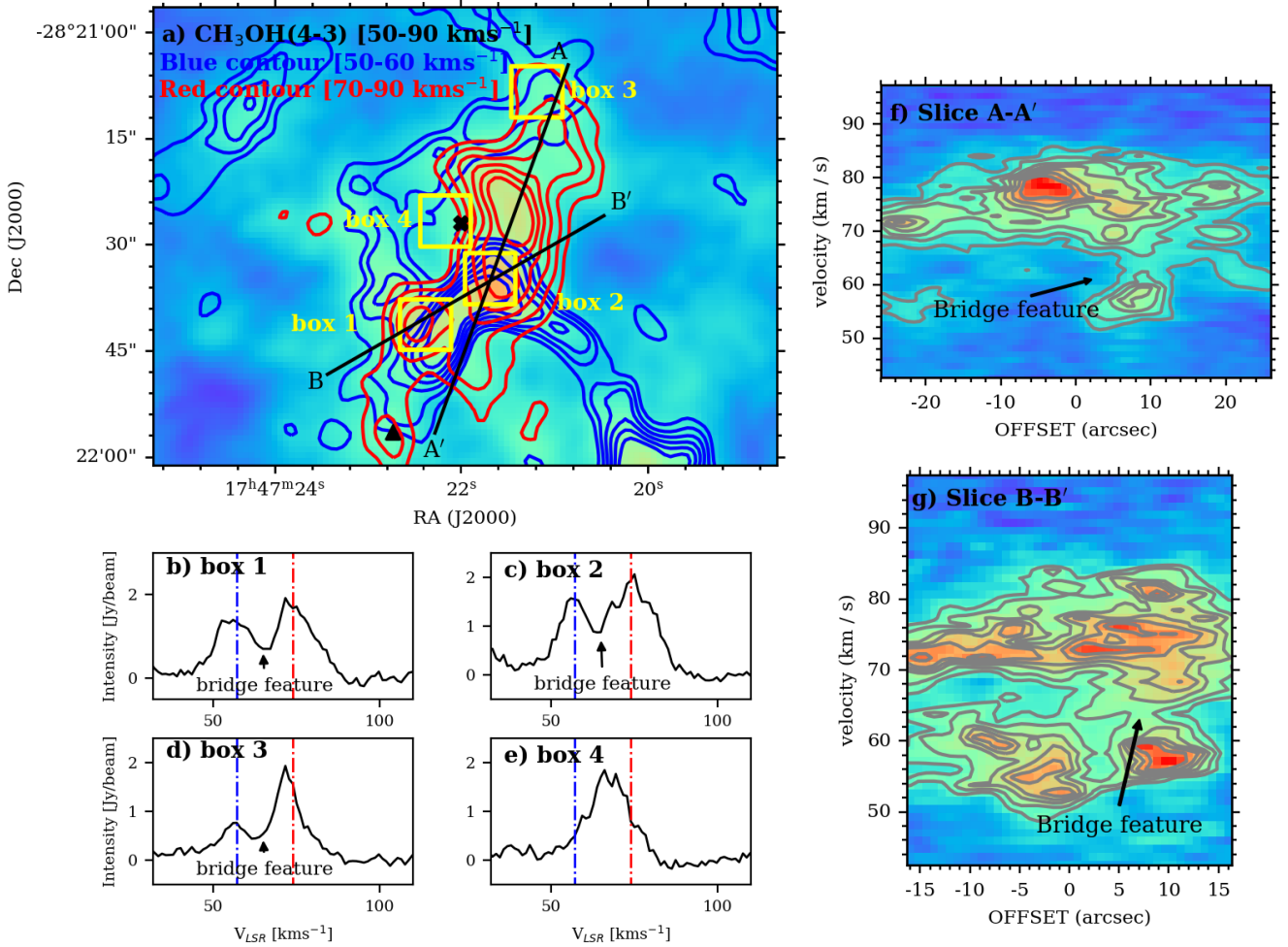


**Figure 5.** (a) Integrated  $\text{CH}_3\text{OH}(4-3)$  emission map (colour scale) over velocity range of 50-90  $\text{km s}^{-1}$  around G+0.693. The blue and red contours indicate the blue-shifted component (50-60  $\text{km s}^{-1}$ ) and the red-shifted component (70-90  $\text{km s}^{-1}$ ) respectively. The yellow boxes (box 1 to box 4) denote the small areas that are used to obtain an average molecular spectra. Solid lines denoted with A-A' and B-B' represents the axis where a position-velocity diagram is extracted. (b)-(e) The spectra of  $\text{CH}_3\text{OH}(4-3)$  averaged over the corresponding small areas (i.e. box 1 to box 4; see highlighted boxes in Figure 5(a)). A blue and red vertical broken line indicates the peak velocity of the blue-shifted and the red-shifted components respectively. The bridge features at the intermediate velocity range are annotated by the arrows. (f) A position-velocity diagram along the axis A-A' as shown in Figure 5(a) with a 3-pixel wide slit at P.A.=160°. (g) A position-velocity diagram along the axis B-B' as shown in Figure 5(a) with a 3-pixel wide slit at P.A.=120°.

The 36 GHz and 44 GHz methanol masers have already been reported in the Sgr B2 region (Liechti & Wilson 1996; Jones et al. 2011). The emission of these two lines are shown to have different spatial distribution, in particular the 36 GHz line shows its strongest emission toward the position of G+0.693 whilst the peak of 44 GHz emission appears near Sgr B2N and Sgr B2M (see Figure 4 in Jones et al. 2011). For the line profile obtained in this study, multiple narrow velocity features are present in both 36 GHz and 44 GHz lines which are likely associated to inhomogeneities in the shocked gas. They also consist of broad ( $\sim 10$ -20  $\text{km s}^{-1}$ ) components as well as narrow ( $< 5$   $\text{km s}^{-1}$ ) spike-like ones. However the two line profiles seem to be complementary in velocity, the brightest peak of 36 GHz line is offset with respect to the 44 GHz line. This possibly indicates that the masers are arising from different regions of the cloud. Furthermore, the 36 GHz emission appears much more prominent than the 44 GHz line toward G+0.693. This is rather unusual since ma-

jority of the sources with both 36 GHz and 44 GHz lines detected are enhanced in 44 GHz (Voronkov et al. 2014).

By using the multiple  $\text{CH}_3\text{OH}$  transitions covered in our dataset, we attempt to constrain the physical properties of the gas that is experiencing masering amplification by using the non-LTE radiative transfer code RADEX (Van der Tak et al. 2007) with collision rates from Rabli & Flower (2010). To run RADEX, we assume a uniform spherical geometry and a cosmic microwave background radiation temperature of  $T = 2.73$  K. Given that the molecular emission is extended, the beam-filling factor is assumed to be unity. The  $\text{CH}_3\text{OH}$  linewidth and column density were fixed to  $\delta v = 20$   $\text{km s}^{-1}$  which is the derived median values of  $\text{CH}_3\text{OH}$  linewidth from 5 different transitions detected in G+0.693 (Requena-Torres et al. 2008); and  $N_{\text{CH}_3\text{OH}} = 2.1 \times 10^{16}$   $\text{cm}^{-2}$  which is calculated from the derived  $\text{CH}_3\text{OH}$  abundance ( $5 \times 10^{-7}$ ) with respect to  $\text{H}_2$  by adopting their derived  $\text{H}_2$  column density =  $4.1 \times 10^{22}$   $\text{cm}^{-2}$  (Requena-Torres



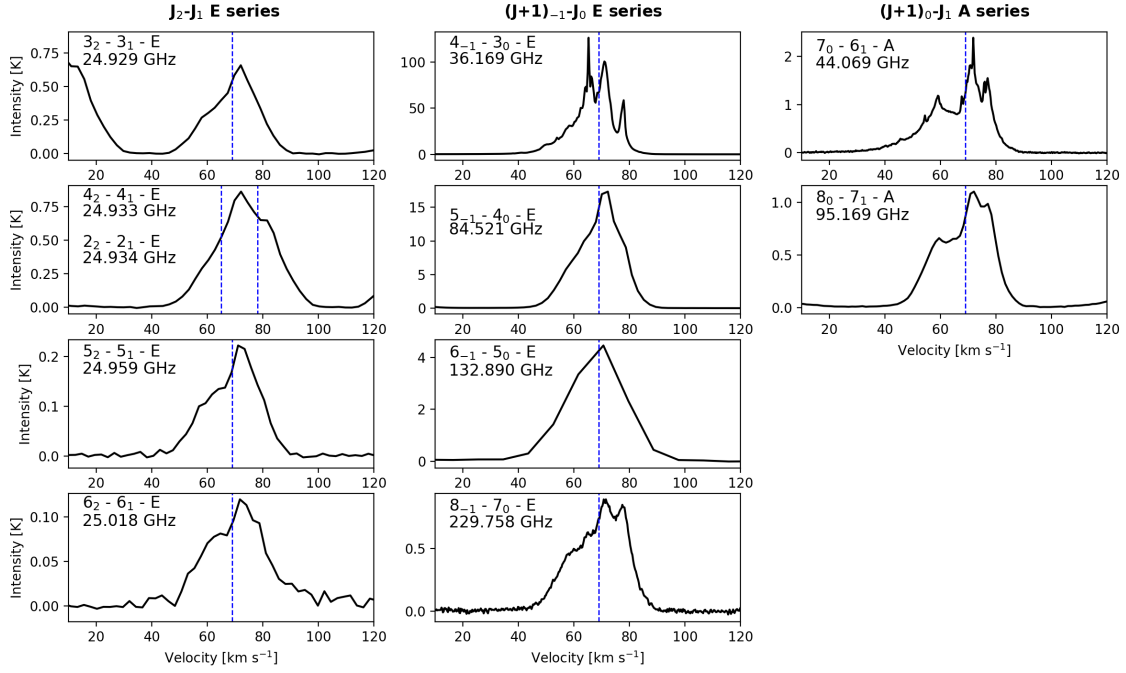


**Figure 6.** Spectra of the class I methanol masers detected toward G+0.693. The blue dashed line denote the central radial velocity of G+0.693. The corresponding transition and frequency is indicated at the top left corner in each panel.

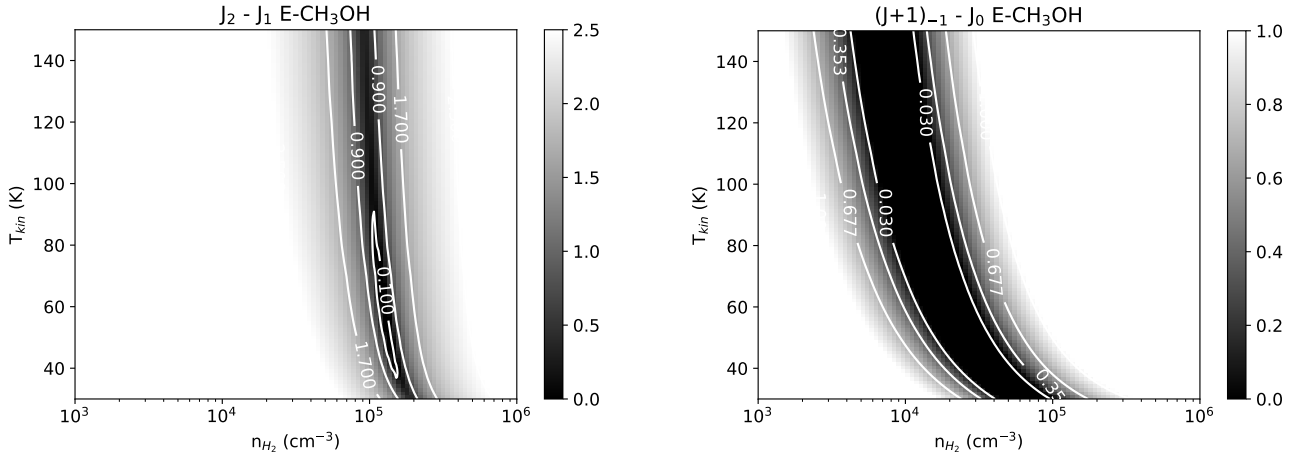


**Figure 7.** Log of  $\chi^2$  fit results from RADEX analysis for  $J_2 - J_1$  E series and  $(J+1)_{-1} - J_0$  E series of class I methanol masers for a wide range of kinetic temperatures and  $H_2$  densities. Darker regions show a lower  $\chi^2$  which indicates better fits than lighter regions.

et al. 2008). The model grids encompass  $H_2$  densities in the range of  $n_{H_2} = 10^3 - 10^6 \text{ cm}^{-3}$  and kinetic temperatures  $T_{kin}$  range between 30 - 150 K. The line intensities generated by RADEX for all transitions can then be compared to the measured line intensities. A reduced  $\chi^2$  fitting was conducted for each model to determine the best fit. Our results are displayed in Figure 7. Although both  $J_2 - J_1$  and  $(J+1)_{-1} - J_0$  series belong to E- $CH_3OH$  species, RADEX does not converge when all the transitions are considered simultaneously. Indeed, different excitation conditions are required to reproduce the  $CH_3OH$  maser emissions from the two series.

For  $J_2 - J_1$  E series, we obtain the minimum reduced  $\chi^2$  for a density  $\sim 1.0 \times 10^5 \text{ cm}^{-3}$  and temperature in a range of 40 - 90 K. While for  $(J+1)_{-1} - J_0$  E series, the density is well fit between  $10^4 - 10^5 \text{ cm}^{-3}$  but the temperature is poorly constrained as low  $\chi^2$  values are found across the temperature range. With only two transitions detected for  $(J+1)_0 - J_1$  A series, the models cannot provide constraints on density and temperature. In general, our results agree with the finding of Leurini et al. (2016) in which the class I masers in the 25 GHz series i.e. the  $J_2 - J_1$  E series maser at higher densities than other lines. They are also consistent with the physical

conditions of typical Galactic centre molecular clouds with little or no star formation activity. The difference in excitation conditions support the idea that these maser series likely arise from different parts of the cloud. It is noteworthy that the methanol emission at 218 GHz ( $5_2-4_1$ ) which is an analogue of the 25 GHz series (Voronkov et al. 2012; Hunter et al. 2014) does not show inversion population in our calculation. This means that the 218 GHz line is quasi-thermal and it reflects the gas distribution in G+0.693.

## 4 DISCUSSIONS

### 4.1 Comparisons with observations in Sgr B2 region

Toward the Sgr B2 molecular cloud complex, Hasegawa et al. (1994) discovered the characteristic kinematic features of a 'hole' and a 'clump' region in  $^{13}\text{CO}$  distribution (see the sketch in Figure 8). The 'hole' refers to a shell-like structure with an inner cavity roughly  $5'$  in size and that appears for the emission integrated between velocities of 40 - 50  $\text{km s}^{-1}$ . The 'clump' refers to a prominent emission peak that shows up at the same position with similar morphology by integrating over the velocity range of 70 - 80  $\text{km s}^{-1}$ . As illustrated in Figure 8, G+0.693 is located within the 'hole' and 'clump' region. Consistently, little molecular emission are present in our study at the velocity range of 40-50  $\text{km s}^{-1}$  while the molecular emission peak is found at 70-80  $\text{km s}^{-1}$ . However, our dataset does not cover a large enough area to reveal the morphological complementarity between the 'hole' and the 'clump' features as reported in Hasegawa et al. (1994) and Sato et al. (2000). In order to explain the existence of these features, a cloud-cloud collision scenario has been put forward (Hasegawa et al. 1994). The 'hole' at velocities between 40 and 50  $\text{km s}^{-1}$  is presumably created by a dense clump with velocities between 70 and 80  $\text{km s}^{-1}$  that is plowing into a more extended molecular cloud, resulting in a cloud-cloud collision with an inclination to the northeast with respect to the line of sight, producing strong shocks in the interface region. This hypothesis is further supported by Sato et al. (2000). In such case, G+0.693 is possibly situated near the northern interface where the interaction would be expected to be stronger. Indeed, our observations seems to draw the same picture where the red-shifted components at velocities between 70 and 80  $\text{km s}^{-1}$  (corresponding to the 'clump') interacts with the blue-shifted components at velocities between 50 and 60  $\text{km s}^{-1}$ , causing the deficient emission (the 'hole') observed at velocities between 40 and 50  $\text{km s}^{-1}$ . And the shock tracers detected toward G+0.693 likely trace the shock associated with this cloud-cloud collision.

The gas kinematics of the Sgr B2 region have recently been revisited by Henshaw et al. (2016) in which a conical structure is observed in position-position-velocity (PPV) space with HNC. Figure 8 only displays the base and the tip of this conical structure. In comparison to the 'hole' and the 'clump' features, the PPV-structure of Sgr B2 is continuous, i.e. there is no discontinuity between the velocity of the 'hole' and the emission peak. As a consequence, the impression of a hole feature can be seen by integrating over different velocity ranges except for the emission peak due to the conical structure, but not only at velocity of 40-50

$\text{km s}^{-1}$  as previously observed. In addition, Henshaw et al. (2016) founds that the emission peak lies between 60-70  $\text{km s}^{-1}$ , does not correspond to the 'clump' at 70-80  $\text{km s}^{-1}$ . And the molecular emission between 70-100  $\text{km s}^{-1}$  is considered to be related to an extended high-velocity feature present at the north-east region beyond Sgr B2 complex.

This conical structure however, can have various interpretations. One could argue that the cone shape is in fact the result of a high-velocity cloud that is punching through a cloud at lower velocity, supporting the cloud-cloud collision scenario proposed by Hasegawa et al. (1994). The appearance of a hole can be easily created due to the conical profile and/or self-absorption of molecular line profile. Indeed, the  $^{13}\text{CO}$  emission used in Hasegawa et al. (1994) is known to be affected by self-absorption (Sato et al. 2000). Furthermore, the tip of the conical structure almost overlaps with the position of G+0.693 (see Figure 8) which implies the same idea that G+0.693 is expected to be affected by the shock from the nearby cloud-cloud collision. On the contrary, such conical structure is speculated to be closely linked to the orbital dynamics of the gas in the CMZ (Kruijssen et al. 2019). In the models described by Kruijssen et al. (2015); Henshaw et al. (2016); Kruijssen et al. (2019), the gas in the inner CMZ ( $R < 120$  pc) is represented by open stream(s) following an eccentric orbit. Sgr B2 resides close to the apocenter where the orbit curves off, causing the superposition of clouds along the line of sight (see Figure 8). The conical structure observed is suggested to be naturally created in this manner without invoking the event of cloud-cloud collision.

In spite of these, several shell-like features are identified by Tsuboi et al. (2015, labelled as Shells 1-6) in the Sgr B2 complex in SiO and  $\text{H}^{13}\text{CO}^+$ . The detailed parameters of these shells are given in Table 4 of their paper. In Figure 8, it shows that G+0.693 is close to the rim of Shell 2 and Shell 3, possibly residing at the region where the two shells intersect. Although both Shell 2 and Shell 3 are proposed to be expanding shells, the former is considered to be originated from successive supernovae in the CMZ while the latter is postulated to be the result of an ongoing cloud-cloud collision with the timescale of  $\sim 10^5$  years (see also Martín-Pintado et al. 1999, on expanding shell in  $\text{NH}_3$ ).

### 4.2 Scenario of an early cloud-cloud collision?

Our present observations have revealed the following pieces of evidence about the gas kinematics toward G+0.693.

- From the velocity channel maps, two velocity components 50-60  $\text{km s}^{-1}$  and 70-90  $\text{km s}^{-1}$  are identified.
- The distribution of two components overlaps toward the southern and northern part while the middle part is spatially separated.
- In the position-velocity diagram, the red-shifted component and blue-shifted component are connected by a bridge feature.

At a glance, Figure 5(a) suggests that two clouds are likely interacting, possibly colliding against each other. Hence in the following, we will interpret these observational features by making comparisons with the common observational and theoretical signatures characteristic of the cloud-cloud collision scenario. As one of the outcomes of cloud-

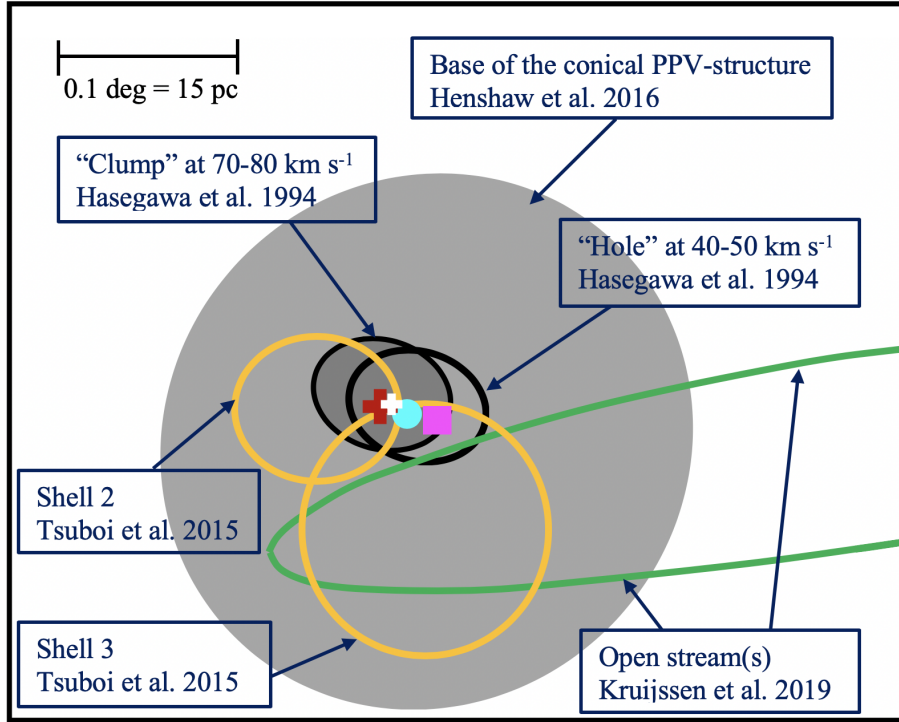


**Figure 8.** A sketch of different observed kinematic features toward G+0.693 region. G+0.693, Sgr B2N, and Sgr B2M are denoted by red cross, cyan circle, and magenta square respectively. White cross and grey circle indicate respectively the tip and the base of the conical PPV-structure reported in Henshaw et al. (2016). Black and shaded ellipse refer to the ‘hole’ and the ‘clump’ features observed in Hasegawa et al. (1994). Orange circles denote the expanding shell 2 and 3 in Tsuboi et al. (2015). Green arcs denote the open stream(s) proposed by Kruijssen et al. (2019).

cloud collision, complementary distribution between two colliding clouds at distinct velocities is expected (Habe & Ohta 1992; Anathpindika 2010; Takahira et al. 2014; Torii et al. 2017; Fukui et al. 2018b). Such complementary distribution is presented particularly between colliding clouds with different sizes in which the smaller cloud creates a cavity in the larger cloud. From the model prediction of collisions between two spheres of different sizes, Figure 6 in Takahira et al. (2014) presented the snapshot of surface density plots of the collision model at different relative velocities. The complementary distribution that is accounted for by the cavity is determined by the size as well as the travel distance of the smaller cloud since the initiation of the collision. In addition, depending on the angle of the relative motion to the line of sight ( $\theta$ ), the smaller cloud can be coincident ( $\theta=0$ ) or displaced ( $\theta \neq 0$ ) with the intensity becoming depressed in the molecular distribution at the velocity of the larger cloud (Fukui et al. 2018b).

In the case of G+0.693, the two velocity components do not show clear complementary distribution but overlap with each other for most part of the cloud. Comparing our results with the collision models of Takahira et al. (2014), this may indicate the collision have just been initiated and the cavity has not yet been created by the smaller cloud. Several observations toward young high-mass star-forming regions that are proposed to be at early stage of cloud-cloud collisions also showed less or non-existent complementary gas distribution between the colliding clouds (e.g. Fukui et al. 2016, 2018a; Hayashi et al. 2020).

Another observational support of cloud-cloud collision is the presence of the bridge feature. It represents the shocked interface layer in-between the two clouds and it manifests itself as a velocity component connecting the two clouds at the intermediate velocity in a position-velocity diagram. Haworth et al. (2015a,b) presented synthetic position-velocity diagrams based on hydrodynamical simulations from Takahira et al. (2014) and Shima et al. (2016). Considering the velocity separation of  $\sim 20 \text{ km s}^{-1}$  between two clouds identified in G+0.693, the bridge feature revealed in position velocity diagram (Figure 5 (f) and (g)) seems to be consistent with snapshot of these diagrams taken between 0.4 Myr and 2 Myr after the onset of the collision (see Figure 7 in Haworth et al. 2015a). This agrees with the absence of complementary distribution in our observations as the collision has just begun and the bridge feature has started to form. Nevertheless, the strong enhancement of SiO emission toward G+0.693 may serve as evidence for supersonic shock waves that are generated at the beginning of a collision (e.g. Hasegawa et al. 1994; Tsuboi et al. 2015).

The detection of bright class I methanol masers toward G+0.693 also strengthens the scenario of cloud-cloud collision. They usually act as tracers of interstellar shocked gas. Particularly, studies have found class I methanol masers to be excited in the shocked regions associated with molecular outflows (e.g. Kurtz et al. 2004; Voronkov et al. 2006; Cyganowski et al. 2009), interaction between supernova remnants and molecular clouds (e.g. Sjouwerman et al. 2010; Pihlström et al. 2011; Frail 2011; Pihlström et al. 2014), in-



interaction between expanding H II regions and the ambient molecular environment (e.g. Voronkov et al. 2010, 2012) and cloud-cloud collisions (e.g. Sobolev 1992; Salii et al. 2002). In the CMZ, the interaction between enhanced cosmic rays and molecular gas can also be responsible for class I methanol masers (Yusef-Zadeh et al. 2013).

Opposite to star forming regions with protostellar outflows, where the 44 GHz line is usually found to be stronger than the other methanol maser transitions (e.g. Pratap et al. 2008; Voronkov et al. 2014), the 36 GHz line appears to be more than an order of magnitude brighter than the 44 GHz transition toward G+0.693. Besides, no studies so far have reported in G+0.693 accompanying emission from 6.7 GHz class II masers, 22 GHz water masers and other transitions that are typically found in star-forming regions (Ladeyschikov et al. 2019; Lu et al. 2019a). All this suggests that molecular outflows and expanding H II regions can hardly be responsible for the methanol masers in G+0.693. Although the 36 GHz line is observed to be more intense than the 44 GHz line in regions shocked by supernova remnant-molecular cloud interactions (e.g. Pihlström et al. 2011, 2014), they are expected to be accompanied by OH masers at 1720 MHz (e.g. Yusef-Zadeh et al. 2003; Frail 2011). Toward G+0.693, the absence of OH masers as well as other observational signatures of supernova remnant-molecular cloud interaction summarised by Slane et al. (2015) indicate that such interaction is unlikely the mechanism to produce methanol masers detected in this study.

From our available observational data, one remarkable result to note is that the strongest integrated intensity over velocity between 70 - 80 km s<sup>-1</sup> (see column 3 in Figure 4 of shock tracers SiO, CH<sub>3</sub>OH, HNC and SO superimpose spatially with the location where the most intense 36 GHz and 84 GHz methanol emission is observed by Liechti & Wilson (1996), Jones et al. (2008), and Jones et al. (2011) (roughly at  $\alpha(J2000.0) = 17^h 47^m 21^s$  and  $\delta(J2000.0) = -28^\circ 21' 23''$ ). This is specifically the position located right above box 2 where the blue-shifted component interacts with the red-shifted component in Figure 5. The enhanced abundance of SiO and HNC observed toward G+0.693 is suggested to be produced by large-scale low-velocity shocks present in the region (Martín-Pintado et al. 1997; Minh & Irvine 2006; Martín et al. 2008). From this perspective, shocks generated by the collisions between two clouds are favoured in our case to provide the excitation responsible for the class I methanol maser.

A similar case is reported in the extragalactic source NGC 253 (Ellingsen et al. 2017). Other than detecting 36 GHz line about two orders of magnitude higher than the 44 GHz line, the integrated intensity of SiO is shown to be coincident with that of the 36 GHz methanol emission. The authors proposed that the methanol maser emission originates in a region with a significant rate of cloud-cloud collisions. The alike interpretation of class I methanol masers between G+0.693 and NGC 253 is consistent with previous studies that show a striking similarity in chemical abundances and excitation conditions between the two regions (Martín et al. 2006; Armijos-Abendaño et al. 2015).

### 4.3 Origin of the rich chemistry in G+0.693

G+0.693 is a molecular cloud in the Galactic centre that exhibits a very rich chemistry, comparable to that observed in star-forming regions in the Galactic disk. However, the SMA and ALMA continuum maps show that G+0.693 does not seem to be associated with any thermal continuum source and the dust temperature ( $\leq 20$  K) is considerably lower than the gas temperature (30 - 150 K). Both of these imply that stellar feedback is likely not responsible for the high abundances of molecular species such as HNC or CH<sub>3</sub>OH measured in this position (e.g. Requena-Torres et al. 2006; Zeng et al. 2018). A low excitation temperature of  $\leq 20$  K has been found for numerous COMs detected toward G+0.693 (e.g. Requena-Torres et al. 2008; Zeng et al. 2018), which can be explained by the low gas density ( $10^4$ - $10^5$  cm<sup>-3</sup>) of the cloud that allows the sub-thermal excitation of COMs.

On the other hand, as a consequence of a cloud-cloud collision, shocks are expected to sputter efficiently the icy grain mantles ejecting molecules formed on grains into the gas phase. Such mechanical process does not only explain the extended distribution of different molecular emission revealed in this study but also the high gas-phase abundance in this region. A large condensation of gas is found to coincide with the position where two velocity components likely interact in G+0.693. In other words, the gas condensation may be formed by the cloud-cloud collision which has enhanced the gas density of the region and the induced shocks would activate the rich chemistry in G+0.693. The RADEX analysis of J<sub>2</sub> - J<sub>1</sub> E series of methanol masers is found to trace higher gas density than (J+1)<sub>-1</sub> - J<sub>0</sub> E series meaning that the collision giving rise to the methanol maser J<sub>2</sub> - J<sub>1</sub> E series is in the higher post-shock density. However spatial distribution of J<sub>2</sub> - J<sub>1</sub> E series is required to confirm the coincidence between the region where this maser originates from within the region where the collision occur. Furthermore, it is natural to assume the physical and chemical properties of the surrounding gas are also modified by the shock driven by this cloud-cloud collision. This is supported by the presence of another molecular condensation that is observed in shock tracers such as SiO, HNC, SO and CH<sub>3</sub>OH by integrating intensity over velocities between 70 - 80 km s<sup>-1</sup>. This position also coincides with that reported for the strong emission of (J+1)<sub>-1</sub> - J<sub>0</sub> E methanol maser. From the RADEX modelling results, we find that the gas kinetic temperature is hard to be constrained which could be due to the E<sub>up</sub> of the detected transitions being lower than the actual T<sub>kin</sub>. It may alternatively indicate this region is not at a constant temperature and this is not surprising in a shocked region where temperature varies rapidly with time and space.

The CMZ in the Galactic centre is rather a complex environment where many energetic phenomenon can play a role the chemistry of the molecular gas. For instance, X-rays and the enhanced cosmic-rays ionisation rates have been invoked to account for some of the abundant COMs detected in G+0.693 (Zeng et al. 2018). All the arguments above emphasise the suggestion that shocks induced by the cloud-cloud collision is likely the most important process responsible for the high level of chemical complexity observed toward G+0.693.

## 5 CONCLUSIONS

For the first time, we have studied the small-scale morphology and kinematics of G+0.693 by using interferometric data in combination with single-dish observations. The major outcomes of the paper are as follow:

- No clear continuum peak is detected in the 1.3 mm continuum map obtained with the SMA, supporting the quiescent nature of G+0.693. This is consistent with previous studies carried out with ALMA at 3 mm (Ginsburg et al. 2016).
- From the SMA spectral line observations and complementary APEX sing-dish data, we found that the general molecular gas distribution toward G+0.693 is extended and elongated in the north-south direction. A molecular condensation is revealed in an offset position from the pointing position of G+0.693 which implies the existence of sub-structure that has not been uncovered previously.
- Two molecular components appear at the velocity ranges of 50-60 km s<sup>-1</sup> and 70-90 km s<sup>-1</sup> as identified from the molecular gas emission of shock tracers such as HNC, SiO, CH<sub>3</sub>OH and HNC. Their integrated emission map and position-velocity diagrams depict observational characteristic of a cloud-cloud collision that has just been initiated.
- A total of 11 transitions from three different series of class I methanol masers are detected toward G+0.693 in our GBT, Yebes 40m and IRAM 30m single-dish data. This type of masers are associated with shock interactions, supporting the idea of a large-scale cloud-cloud collision. We modelled the multiple transitions of J<sub>2</sub> - J<sub>1</sub> E series and (J+1)<sub>-1</sub> - J<sub>0</sub> E series with non-LTE calculations to provide constraints on the physical conditions in G+0.693. We obtained different excitation conditions for two series which may indicate they arise from different regions in G+0.693. The analysis also provides a strong constraint on the gas density which is between 10<sup>4</sup>-10<sup>5</sup> cm<sup>-3</sup> but not on the gas temperature. The large range of the gas temperature obtained from the models may be explained by the idea that the class I methanol masers originate from a shocked region which is presumably affected by the event of a cloud-cloud collision.
- The characteristics of the class I methanol masers studied in G+0.693 appear to share remarkable similarities with the class I masers detected in the extragalactic source NGC 253, which has also been proposed to be experiencing cloud-cloud collisions in its nuclear starburst.

In summary, our results are consistent with the proposed idea that the chemistry of G+0.693 is dominated by low-velocity shocks which are likely originated from the occurrence of a cloud-cloud collision. If this holds, it is expected that such collision would enhance the gas density to levels at which star formation may proceed.

## ACKNOWLEDGEMENTS

We wish to thank the anonymous referee for his/her very useful comments that helped to improve this article. We would like to thank Adam Ginsburg (University of Florida) for providing the ALMA image. Based on observations with the 40-m radio telescope of the National Geographic Institute of Spain (IGN) at Yebes Observa-

tory (project number 20A008). Yebes Observatory acknowledges the ERC for funding support under grant ERC-2013-Syg-610256-NANOCOSMOS. S. Z acknowledges support through a Principal's studentship funded by Queen Mary University of London, the visiting student program funded by Harvard-Smithsonian Center for Astrophysics. I.J.-S. and J.M.-P. have received partial support from the Spanish FEDER under project number ESP2017-86582-C4-1-R. V.M.R. has received funding from the European Union's Horizon 2020 research and innovation programme under the Marie Skłodowska-Curie grant agreement No 664931. X.L. was financially supported by JSPS KAKENHI grants No. 18K13589 & 20K14528

## DATA AVAILABILITY

The data underlying this article will be shared on reasonable request to the corresponding author.

## REFERENCES

- Anathpindika S. V., 2010, *MNRAS*, **405**, 1431  
 Arce H. G., Sargent A. I., 2006, *ApJ*, **646**, 1070  
 Armijos-Abendaño J., Martín-Pintado J., Requena-Torres M. A., Martín S., Rodríguez-Franco A., 2015, *MNRAS*, **446**, 3842  
 Bally J., Stark A. A., Wilson R. W., Henkel C., 1987a, *ApJS*, **65**, 13  
 Bally J., Stark A. A., Wilson R. W., 1987b, in Peimbert M., Jugaku J., eds, IAU Symposium Vol. 115, Star Forming Regions. p. 550  
 Battersby C., et al., 2017, in Crocker R. M., Longmore S. N., Bicknell G. V., eds, IAU Symposium Vol. 322, The Multi-Messenger Astrophysics of the Galactic Centre. pp 90–94 ([arXiv:1610.05805](https://arxiv.org/abs/1610.05805)), doi:10.1017/S1743921316012266  
 Battersby C., et al., 2020, arXiv e-prints, [p. arXiv:2007.05023](https://arxiv.org/abs/2007.05023)  
 Cernicharo J., 1985, Internal IRAM Report (Granada: IRAM)  
 Cyganowski C. J., Brogan C. L., Hunter T. R., Churchwell E., 2009, *ApJ*, **702**, 1615  
 De Vicente P., Martín-Pintado J., Neri R., Colom P., 2000, *A&A*, **361**, 1058  
 Ellingsen S. P., Chen X., Breen S. L., Qiao H. H., 2017, *MNRAS*, **472**, 604  
 Endres C. P., Schlemmer S., Schilke P., Stutzki J., Müller H. S. P., 2016, *Journal of Molecular Spectroscopy*, **327**, 95  
 Frail D. A., 2011, Mem. Soc. Astron. Italiana, **82**, 703  
 Fukui Y., et al., 2016, *ApJ*, **820**, 26  
 Fukui Y., et al., 2018a, *PASJ*, **70**, S41  
 Fukui Y., et al., 2018b, *ApJ*, **859**, 166  
 Ginsburg A., et al., 2016, *A&A*, **586**, A50  
 Ginsburg A., et al., 2018, *ApJ*, **853**, 171  
 Goto M., Indriolo N., Geballe T. R., Usuda T., 2013, *Journal of Physical Chemistry A*, **117**, 9919  
 Guesten R., Henkel C., 1983, *A&A*, **125**, 136  
 Guesten R., Walmsley C. M., Ungerechts H., Churchwell E., 1985, *A&A*, **142**, 381  
 Habe A., Ohta K., 1992, *PASJ*, **44**, 203  
 Hasegawa T., Sato F., Whiteoak J. B., Miyawaki R., 1994, *ApJ*, **429**, L77  
 Hasegawa T., Arai T., Yamaguchi N., Sato F., 2008, *Ap&SS*, **313**, 91  
 Haworth T. J., et al., 2015a, *MNRAS*, **450**, 10  
 Haworth T. J., Shima K., Tasker E. J., Fukui Y., Torii K., Dale J. E., Takahira K., Habe A., 2015b, *MNRAS*, **454**, 1634  
 Hayashi K., et al., 2020, arXiv e-prints, [p. arXiv:2005.07933](https://arxiv.org/abs/2005.07933)

- Henshaw J. D., et al., 2016, *MNRAS*, **457**, 2675
- Huettemeister S., Wilson T. L., Bania T. M., Martín-Pintado J., 1993, *A&A*, **280**, 255
- Hunter T. R., Brogan C. L., Cyganowski C. J., Young K. H., 2014, *ApJ*, **788**, 187
- Jiménez-Serra I., Martín-Pintado J., Rodríguez-Franco A., Chandler C., Comito C., Schilke P., 2007, *ApJ*, **661**, L187
- Jiménez-Serra I., Caselli P., Martín-Pintado J., Hartquist T. W., 2008, *A&A*, **482**, 549
- Jiménez-Serra I., Martín-Pintado J., Caselli P., Martín S., Rodríguez-Franco A., Chandler C., Winters J. M., 2009, *ApJ*, **703**, L157
- Jimenez-Serra I., et al., 2020, arXiv e-prints, p. [arXiv:2004.07834](https://arxiv.org/abs/2004.07834)
- Jones P. A., et al., 2008, *MNRAS*, **386**, 117
- Jones P. A., Burton M. G., Tothill N. F. H., Cunningham M. R., 2011, *MNRAS*, **411**, 2293
- Kauffmann J., Pillai T., Zhang Q., Menten K. M., Goldsmith P. F., Lu X., Guzmán A. E., Schmiedeke A., 2017, *A&A*, **603**, A90
- Koyama K., Awaki H., Kunieda H., Takano S., Tawara Y., 1989, *Nature*, **339**, 603
- Krieger N., et al., 2017, *ApJ*, **850**, 77
- Kruijssen J. M. D., Dale J. E., Longmore S. N., 2015, *MNRAS*, **447**, 1059
- Kruijssen J. M. D., et al., 2019, *MNRAS*, **484**, 5734
- Kurtz S., Hofner P., Álvarez C. V., 2004, *ApJS*, **155**, 149
- Ladeyschikov D. A., Bayandina O. S., Sobolev A. M., 2019, *AJ*, **158**, 233
- Laurini S., Menten K. M., Walmsley C. M., 2016, *A&A*, **592**, A31
- Liechti S., Wilson T. L., 1996, *A&A*, **314**, 615
- Longmore S. N., et al., 2013, *MNRAS*, **429**, 987
- Lu X., et al., 2019a, *ApJS*, **244**, 35
- Lu X., et al., 2019b, *ApJ*, **872**, 171
- Martín-Pintado J., de Vicente P., Fuente A., Planesas P., 1997, *ApJ*, **482**, L45
- Martín-Pintado J., Gaume R. A., Rodríguez-Fernández N., de Vicente P., Wilson T. L., 1999, *ApJ*, **519**, 667
- Martín-Pintado J., Jiménez-Serra I., Rodríguez-Franco A., Martín S., Thum C., 2005, *ApJ*, **628**, L61
- Martín S., Mauersberger R., Martín-Pintado J., Henkel C., García-Burillo S., 2006, *ApJS*, **164**, 450
- Martín S., Requena-Torres M. A., Martín-Pintado J., Mauersberger R., 2008, *ApJ*, **678**, 245
- McMullin J. P., Waters B., Schiebel D., Young W., Golap K., 2007, in Shaw R. A., Hill F., Bell D. J., eds, *Astronomical Society of the Pacific Conference Series Vol. 376, Astronomical Data Analysis Software and Systems XVI*. p. 127
- Miao Y., Mehringer D. M., Kuan Y.-J., Snyder L. E., 1995, *ApJ*, **445**, L59
- Mills E. A. C., Ginsburg A., Immer K., Barnes J. M., Wiesenfeld L., Faure A., Morris M. R., Requena-Torres M. A., 2018, *ApJ*, **868**, 7
- Minh Y. C., Irvine W. M., 2006, *New Astron.*, **11**, 594
- Morris M., Serabyn E., 1996, *ARA&A*, **34**, 645
- Müller H. S. P., Thorwirth S., Roth D. A., Winnewisser G., 2001, *A&A*, **370**, L49
- Müller H. S. P., Schlöder F., Stutzki J., Winnewisser G., 2005, *Journal of Molecular Structure*, **742**, 215
- Nagayama T., Omodaka T., Handa T., Toudjima H., Sofue Y., Sawada T., Kobayashi H., Koyama Y., 2009, *PASJ*, **61**, 1023
- Ossenkopf V., Henning T., 1994, *A&A*, **291**, 943
- Ott J., Weiß A., Staveley-Smith L., Henkel C., Meier D. S., 2014, *ApJ*, **785**, 55
- Pardo J. R., Cernicharo J., Serabyn E., 2001, *IEEE Transactions on Antennas and Propagation*, **49**, 1683
- Pickett H. M., Poynter R. L., Cohen E. A., Delitsky M. L., Pearson J. C., Müller H. S. P., 1998, *J. Quant. Spectrosc. & Rad. Transfer*, **60**, 883
- Pihlström Y. M., Sjouwerman L. O., Fish V. L., 2011, *ApJ*, **739**, L21
- Pihlström Y. M., Sjouwerman L. O., Frail D. A., Claussen M. J., Mesler R. A., McEwen B. C., 2014, *AJ*, **147**, 73
- Pratap P., Shute P. A., Keane T. C., Battersby C., Sterling S., 2008, *AJ*, **135**, 1718
- Rabli D., Flower D. R., 2010, *MNRAS*, **406**, 95
- Reid M. J., et al., 2014, *ApJ*, **783**, 130
- Requena-Torres M. A., Martín-Pintado J., Rodríguez-Franco A., Martín S., Rodríguez-Fernández N. J., de Vicente P., 2006, *A&A*, **455**, 971
- Requena-Torres M. A., Martín-Pintado J., Martín S., Morris M. R., 2008, *ApJ*, **672**, 352
- Rivilla V. M., et al., 2018, *MNRAS*, **475**, L30
- Rivilla V. M., et al., 2019, *MNRAS*, **483**, L114
- Rodríguez-Fernández N. J., Martín-Pintado J., de Vicente P., Fuente A., Hüttemeister S., Wilson T. L., Kunze D., 2000, *A&A*, **356**, 695
- Rodríguez-Fernández N. J., Martín-Pintado J., Fuente A., Wilson T. L., 2004, *A&A*, **427**, 217
- Sali S. V., Sobolev A. M., Kalinina N. D., 2002, *Astronomy Reports*, **46**, 955
- Sato F., Hasegawa T., Whiteoak J. B., Miyawaki R., 2000, *ApJ*, **535**, 857
- Sault R. J., Teuben P. J., Wright M. C. H., 1995, in Shaw R. A., Payne H. E., Hayes J. J. E., eds, *Astronomical Society of the Pacific Conference Series Vol. 77, Astronomical Data Analysis Software and Systems IV*. p. 433 ([arXiv:astro-ph/0612759](https://arxiv.org/abs/astro-ph/0612759))
- Schmiedeke A., et al., 2016, *A&A*, **588**, A143
- Shima K., Tasker E. J., Habe A., 2016, in Jablonka P., André P., van der Tak F., eds, *IAU Symposium Vol. 315, From Interstellar Clouds to Star-Forming Galaxies: Universal Processes?*. p. E72, [doi:10.1017/S1743921316008346](https://doi.org/10.1017/S1743921316008346)
- Sjouwerman L. O., Pihlström Y. M., Fish V. L., 2010, *ApJ*, **710**, L111
- Slane P., Bykov A., Ellison D. C., Dubner G., Castro D., 2015, *Space Sci. Rev.*, **188**, 187
- Sobolev A. M., 1992, *Soviet Ast.*, **36**, 590
- Takahira K., Tasker E. J., Habe A., 2014, *ApJ*, **792**, 63
- Torii K., et al., 2017, *ApJ*, **835**, 142
- Tsuboi M., Miyazaki A., Uehara K., 2015, *PASJ*, **67**, 90
- Van der Tak F. F. S., Black J. H., Schöier F. L., Jansen D. J., van Dishoeck E. F., 2007, *A&A*, **468**, 627
- Voronkov M. A., Brooks K. J., Sobolev A. M., Ellingsen S. P., Ostrovskii A. B., Caswell J. L., 2006, *MNRAS*, **373**, 411
- Voronkov M. A., Caswell J. L., Britton T. R., Green J. A., Sobolev A. M., Ellingsen S. P., 2010, *MNRAS*, **408**, 133
- Voronkov M. A., Caswell J. L., Ellingsen S. P., Breen S. L., Britton T. R., Green J. A., Sobolev A. M., Walsh A. J., 2012, in Booth R. S., Vlemmings W. H. T., Humphreys E. M. L., eds, *IAU Symposium Vol. 287, Cosmic Masers - from OH to H0*. pp 433–440 ([arXiv:1203.5492](https://arxiv.org/abs/1203.5492)), [doi:10.1017/S174392131200748X](https://doi.org/10.1017/S174392131200748X)
- Voronkov M. A., Caswell J. L., Ellingsen S. P., Green J. A., Breen S. L., 2014, *MNRAS*, **439**, 2584
- Yusef-Zadeh F., Wardle M., Rho J., Sakano M., 2003, *ApJ*, **585**, 319
- Yusef-Zadeh F., et al., 2013, *ApJ*, **762**, 33
- Zeng S., et al., 2018, *MNRAS*, **478**, 2962
- de Vicente P., et al., 2016, *A&A*, **589**, A74

## APPENDIX A: INTEGRATED MOLECULAR EMISSION MAP AND POSITION-VELOCITY MAP OF HNCO, SIO, AND SO



This paper has been typeset from a  $\text{\LaTeX}$  file prepared by the author.

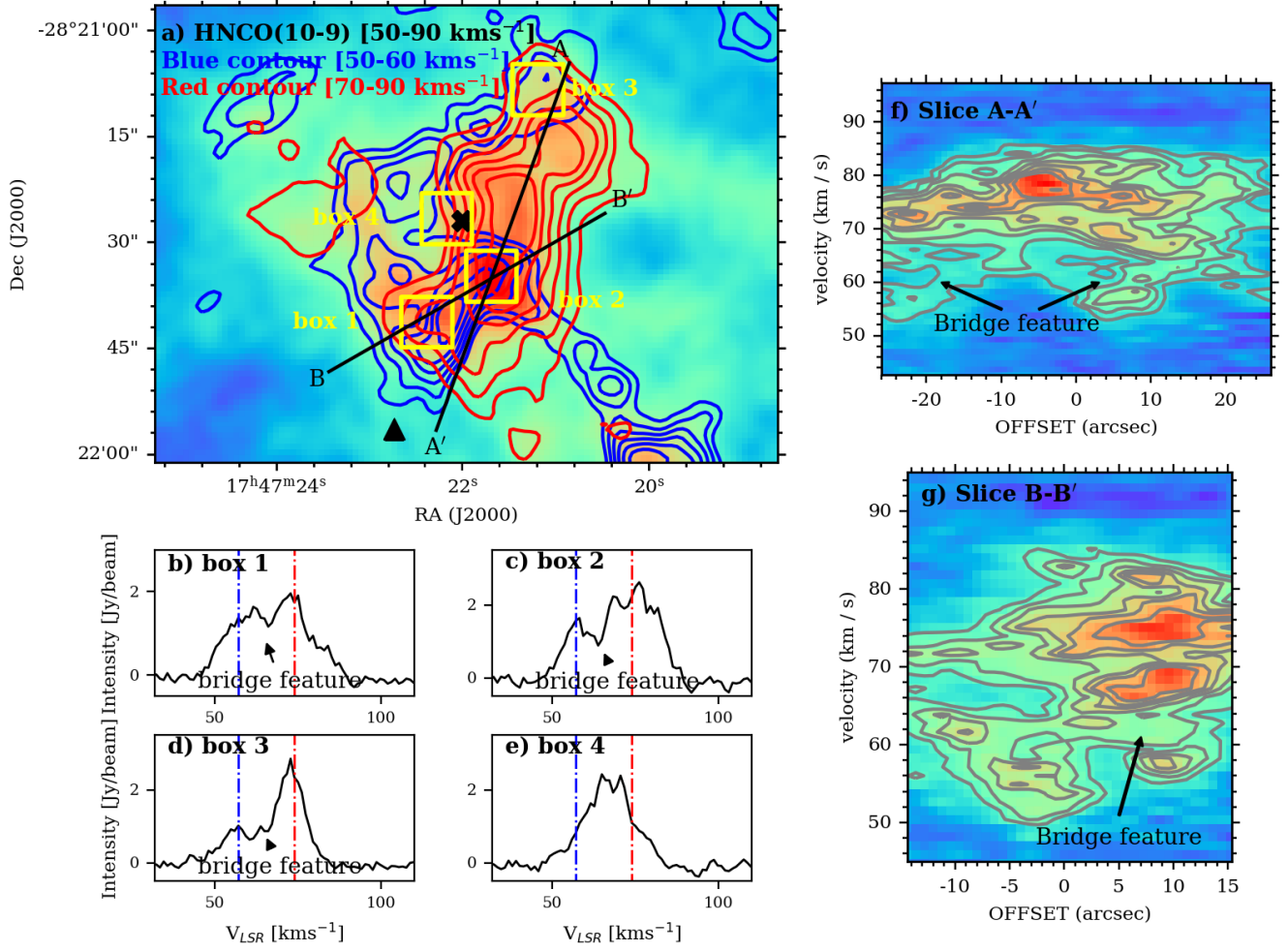


**Figure A1.** HNC(10-9). Caption is the same as Figure 5.

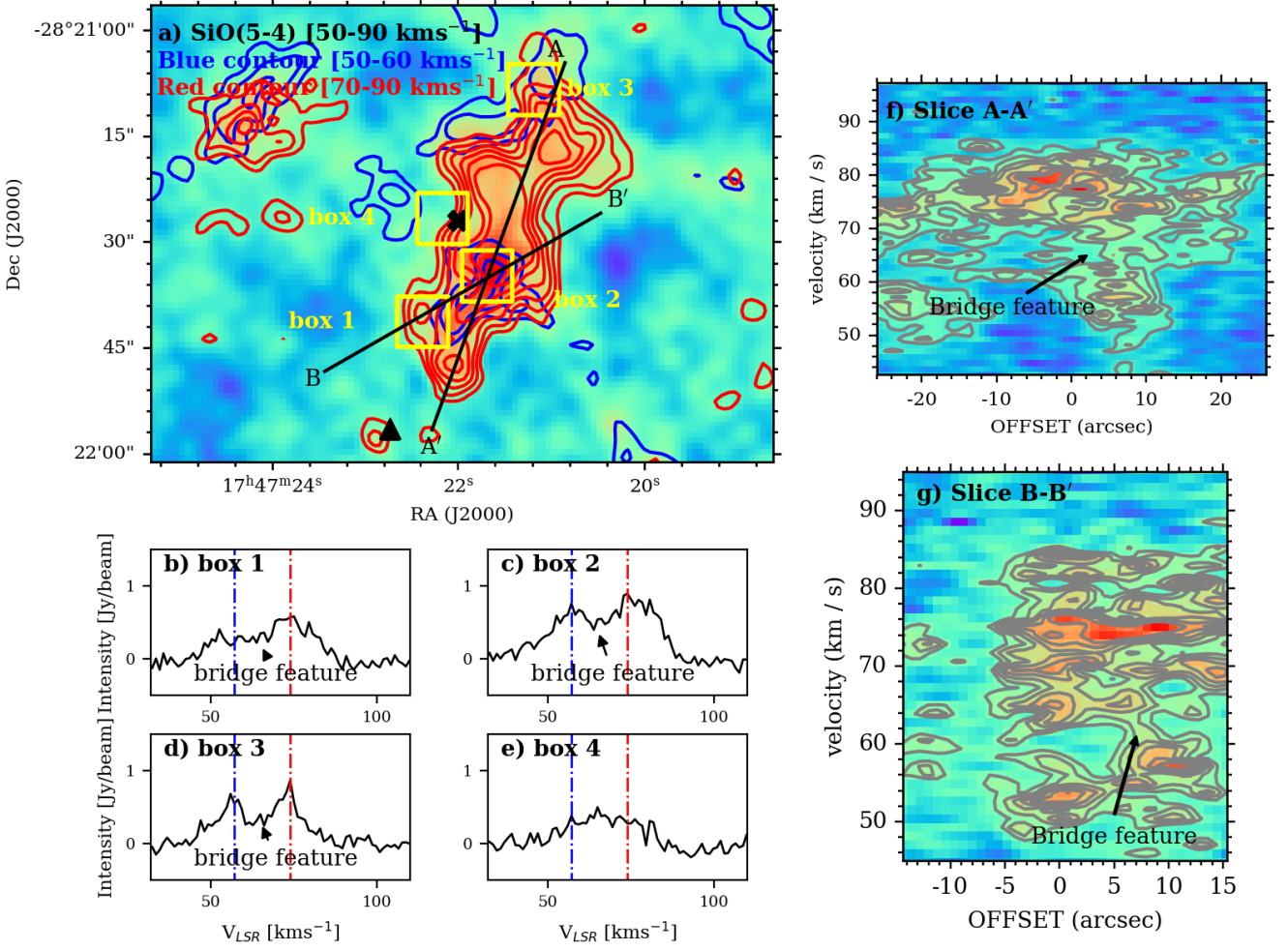


**Figure A2.** SiO(5-4). Caption is the same as Figure 5.



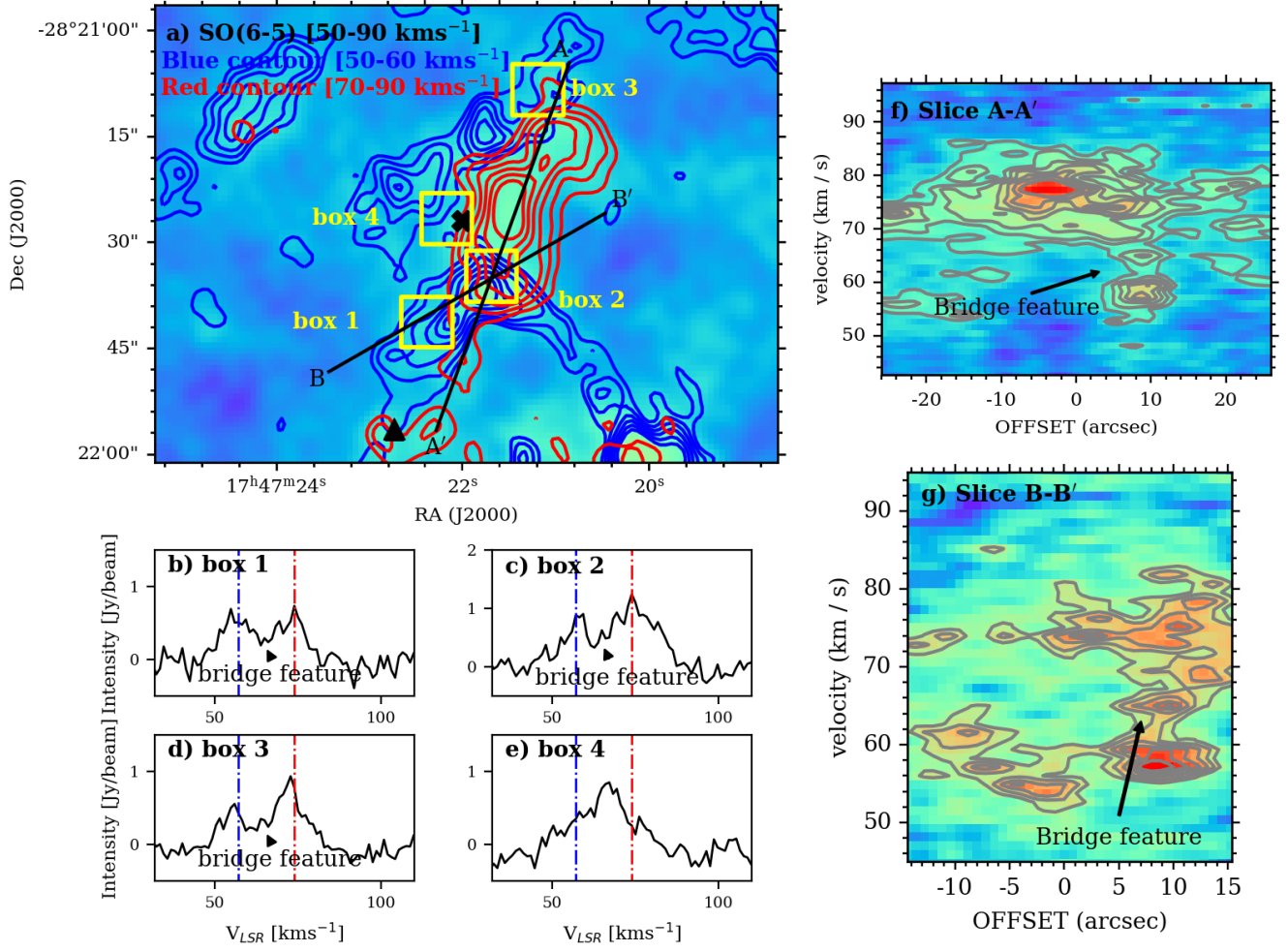


Figure A3. SO(6-5). Caption is the same as Figure 5.